Electronic Properties of Bilayer Graphene Strongly Coupled to Interlayer Stacking and an External Electric Field

Changwon Park,[1] Junga Ryou,[2] Suklyun Hong,[2] Bobby G. Sumpter,[1] Gunn Kim,[2,*] and Mina Yoon[1,†]
[1]*Center for Nanophase Materials Sciences, Oak Ridge National Laboratory, Oak Ridge, Tennessee 37831, USA*
[2]*Department of Physics and Graphene Research Institute, Sejong University, Seoul 143-747, Korea*
(Received 2 October 2014; revised manuscript received 29 January 2015; published 2 July 2015)

Bilayer graphene (BLG) with a tunable band gap appears interesting as an alternative to graphene for practical applications; thus, its transport properties are being actively pursued. Using density functional theory and perturbation analysis, we investigated, under an external electric field, the electronic properties of BLG in various stackings relevant to recently observed complex structures. We established the first phase diagram summarizing the stacking-dependent gap openings of BLG for a given field. We further identified high-density midgap states, localized on grain boundaries, even under a strong field, which can considerably reduce the overall transport gap.

DOI: 10.1103/PhysRevLett.115.015502 PACS numbers: 61.48.Gh, 73.22.Pr, 73.21.Ac

The discovery of graphene has opened new avenues for studying the role of dimensionality on the fundamental properties of materials [1]. Although graphene shows excellent electrical properties [2], the zero band gap of graphene limits its practical application as an electronic device. On the other hand, gap opening is possible in bilayer graphene (BLG), thus making it a very promising material that overcomes graphene's key limitation while retaining many of its interesting properties. For example, massive Dirac fermions in BLG exhibit a band gap tunable by applying a transverse electric field (E field) [3]; this has been demonstrated by optical [4] and electrical transport measurements using dual-gated devices [5,6]. However, these measurements leave a couple of unsolved problems: (i) the origin of unexpectedly small transport gaps that are 2 orders of magnitude smaller than optical gaps [5] and (ii) the origin of anomalous low-temperature (< 2 K) transport behaviors dominated by hopping between localized midgap states, presumably induced from disorder or defects [5,7].

Recent experiments have revealed complex configurations in BLG, including various stacking domains induced by rotational faults and soliton formation [8–10]. While AB stacking is energetically most favorable, the non-AB-stacking region can be stabilized by a minute twist [11] and the stacking boundary [8]. The local stacking configuration is strongly coupled to its electronic structure and its response to an external E field. Therefore, it is critically important, fundamentally and practically, to understand the observed complex stackings and their impact on the overall electronic properties.

In this Letter, using the framework of an effective Hamiltonian based on density functional theory (DFT) and perturbation theory, we analyze gap-opening properties of BLG near the high-symmetry stackings (AA, AA', and AB), under an applied E field. We establish a phase diagram for the stacking-dependent gap openings and further identify grain boundaries containing non-AB stackings as a source for high-density midgap states even under a strong E field. Our findings offer insight to understanding the intrinsic transport properties of BLG.

Our DFT calculations adopt the Perdew-Burke-Ernzerhof version of the exchange-correlation functional [12] and the projector augmented wave method [13] for ionic potentials as implemented in the Vienna *ab initio* simulation package [14]. We obtain interlayer distances between 3.25 (AB) and 3.45 Å (AA) with van der Waals correction [15]; the interlayer distance of all the configurations is fixed at 3.35 Å (unless specified) with practically no changes in their band structures. To ensure an accurate band gap, the 2D DFT band structure near the K point is interpolated [16] by using maximally localized Wannier functions [17]. Effective Hamiltonians are constructed with the obtained hopping parameters truncated to the first-nearest-interlayer hoppings (see details in Supplemental Material [18]).

One of the intriguing properties of BLG is that a change in weak interlayer interaction (which is an order of magnitude smaller than the intralayer coupling strength) accompanied by a modification in stacking configuration can significantly alter the electronic structure around the Fermi level. Figure 1(a) illustrates schematic band structures of the high symmetry stackings, where we define systems with equivalent two sublattices (AA and AA') as sublattice-symmetric systems; otherwise, they are sublattice-asymmetric stackings (AB).

Figure 1(b) shows the atomistic modeling of an experimentally observed domain boundary [9], containing continuous structural transition between two AB-stacking regions. Figure 1(c) plots stacking-dependent potential energy with optimized interlayer distances in the 2D translation vector space, where AB stacking is used as a reference point. The arrow denotes the displacement vector between the left and right domains in Fig. 1(b). Local

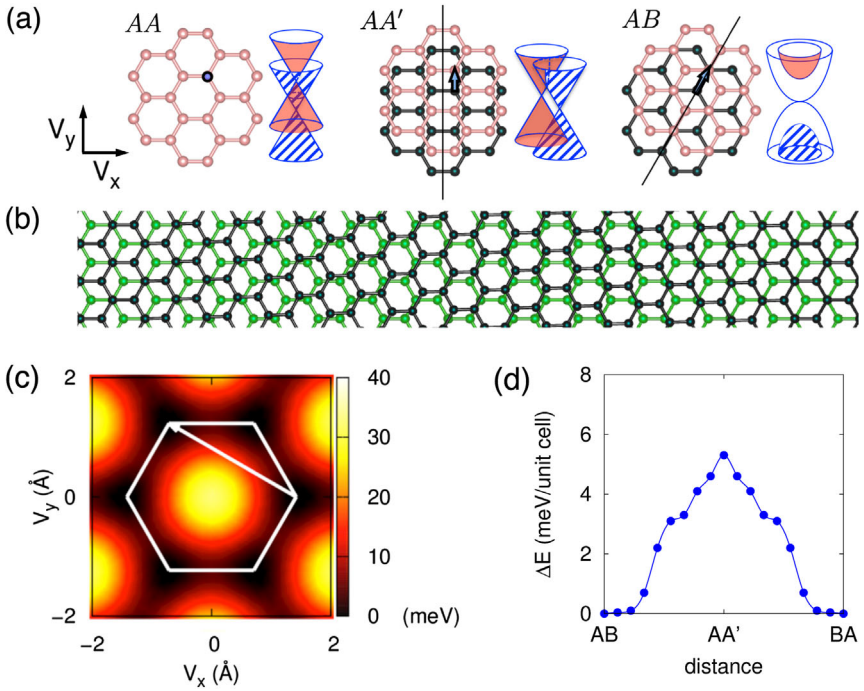

FIG. 1 (color online). (a) Schematic band structures of AA, AA', and AB. The solid lines are reflection planes, where the translation vectors (V_x, V_y) describe the relative displacement between the two layers in the xy plane. (b) Modeling of the two AB-stacking boundary. (c) Stacking-dependent potential energy of BLG per unit cell, where the origin corresponds to AA stacking. A lattice Wigner-Seitz cell is highlighted by the solid white line, and the arrow denotes the displacement vector between the two AB-stacking domains shown in (b). (d) Minimum energy path between the two AB stackings.

stacking configurations of the transition region are distributed on this arrow. To remove this soliton-like boundary, one needs to displace the one on the left or right domain by a displacement vector. The minimum energy path between the two AB stackings lies along the edge of the hexagon with an energy barrier of 5.3 meV/cell [see Fig. 1(d)]. Though this energy barrier seems quite small, the stacking domain should move as a whole so that the high energy barrier, proportional to the domain area ($> 10^4$ unit cell), should be overcome. This explains the observed stability of non-AB-stacking regions.

The gap-opening mechanism of BLG can be highly stacking dependent. We first examine the individual band structures near the high-symmetry stackings and then discuss the gap-opening properties across complex domain boundaries. Their effective Hamiltonian in crystal momentum (k) space can be described by a 4×4 matrix with the basis A_{up}, B_{up}, A_{dn}, and B_{dn}, with A and B sublattice indices and the upper and lower graphene layers for up and dn, respectively. The 2×2 block-diagonal components correspond to the individual graphene layers, while all others describe interlayer coupling. We focus only on the effective Hamiltonian near the K points; band structures around K' can be obtained by applying time-reversal symmetry to those of K.

First we consider the configurations of AA stacking. Neglecting small Bloch phase variations under the Fourier transformations of interlayer coupling, the Hamiltonian of AA stacking around K becomes

$$H_0(k) + \begin{bmatrix} 0 & 0 & \tilde{\gamma}_{AA} & 0 \\ 0 & 0 & 0 & \tilde{\gamma}_{AA} \\ \tilde{\gamma}_{AA} & 0 & 0 & 0 \\ 0 & \tilde{\gamma}_{AA} & 0 & 0 \end{bmatrix}, \quad (1)$$

with $H_0(k)$ defined as

$$H_0(k) \equiv \begin{bmatrix} 0 & \hbar v_F k_+ & 0 & 0 \\ \hbar v_F k_- & 0 & 0 & 0 \\ 0 & 0 & 0 & \hbar v_F k_+ \\ 0 & 0 & \hbar v_F k_- & 0 \end{bmatrix}, \quad (2)$$

where the Fermi velocity multiplied by the reduced Planck constant becomes $\hbar v_F \equiv (\partial E/\partial k) \sim 5.4$ eV Å and $k_\pm \equiv k_y \pm i k_x$. $\tilde{\gamma}_{AA}$ ($= -0.34$ eV) is obtained by the Fourier transformation of the interlayer hopping between A_{up} (B_{up}) and A_{dn} (B_{dn}), γ_{AA} [20]. The hopping parameters between A_{up} (B_{up}) and B_{dn} (A_{dn}) become zero, because the Bloch phases of three interlayer nearest neighbors cancel each other at the K point, $\tilde{\gamma}_{AB} = 0$.

By changing our basis to the bonding and antibonding state of each sublattice, the decoupling of two Dirac cones becomes more transparent:

$$H_0(k) + \begin{bmatrix} \tilde{\gamma}_{AA} & 0 & 0 & 0 \\ 0 & \tilde{\gamma}_{AA} & 0 & 0 \\ 0 & 0 & -\tilde{\gamma}_{AA} & 0 \\ 0 & 0 & 0 & -\tilde{\gamma}_{AA} \end{bmatrix}, \quad (3)$$

a block-diagonal Hamiltonian describing two Dirac cones with energy shift $\pm\tilde{\gamma}_{AA}$ [see Fig. 1(a)].

In the AA'-stacking configuration, one can also explicitly illustrate the decoupling of Dirac cones by changing the basis to interlayer bonding and antibonding of phase-shifted sublattices $[(1/\sqrt{2})A_{\mathrm{up}}(B_{\mathrm{up}}) \pm (1/\sqrt{2})\exp(-2\pi i/3) A_{\mathrm{dn}}(B_{\mathrm{dn}})]$. The Hamiltonian of AA' stacking then becomes

$$H_0(k) + \begin{bmatrix} \tilde{\gamma}_{AA} & -\tilde{\gamma}_{AB} & 0 & 0 \\ -\tilde{\gamma}_{AB} & \tilde{\gamma}_{AA} & 0 & 0 \\ 0 & 0 & -\tilde{\gamma}_{AA} & \tilde{\gamma}_{AB} \\ 0 & 0 & \tilde{\gamma}_{AB} & -\tilde{\gamma}_{AA} \end{bmatrix}, \quad (4)$$

where $\tilde{\gamma}_{AA} = -0.11$ eV and $\tilde{\gamma}_{AB} = -0.22$ eV, corresponding to two Dirac cones separated by 0.22 eV in energy with an additional 0.08 Å^{-1} splitting in k space. Wave functions of the decoupled Dirac cones of both AA and AA' stackings have interlayer antibonding and bonding characteristics, depicted, respectively, in red (shaded) and blue (hatched) in Fig. 1(a).

The Hamiltonian of AB staking can be written as

$$H_0(k) + \begin{bmatrix} 0 & 0 & 0 & \tilde{\gamma}_{AB} \\ 0 & 0 & 0 & 0 \\ 0 & 0 & 0 & 0 \\ \tilde{\gamma}_{AB} & 0 & 0 & 0 \end{bmatrix}; \quad (5)$$

doubly degenerate states at the Fermi level are composed of one sublattice per layer, with no direct coupling between them, and two Dirac points are merged at the K point and split into bonding, antibonding, and nonbonding types [see Fig. 1(a)].

Next, we trace how a small translation or external E field perturbations, can change the band structures near the Fermi level. The AA panel of Fig. 2 summarizes projected (onto $k_\parallel$ and $k_\perp$) band structures for around-AA-stacked graphene. Since interlayer hopping parameters are the same, one cannot generate an on-site energy difference in the 2×2 diagonal block simply by atomic translation, which excludes the direct coupling between two crossing bands (i.e., no gap opening). At the Fermi level, the hole band of one Dirac cone is degenerated along with the electron band of the other Dirac cone. The Fermi surface of the AA stacking is the intersection of two vertically shifted cones. A small translation results in a slight k shift and a coupling of two Dirac cones; a k shift changes the circular intersection into a tilted ellipse, while a coupling introduces energy splitting at the intersection. In general, the energy splitting depends on the angular position of the intersection and becomes zero at two points. These form two crossing points near the Fermi level as shown in the second row. An applied E field introduces an additional energy splitting that also depends on the angular position and becomes zero at two points. When an E field is combined with a sublattice-symmetric translation, their zero splitting points coincide and the system remains metallic. In contrast, with the sublattice-asymmetric translation, each zero coupling point is at a different position and the crossing points disappear (in the inset in the fourth row). Especially when sublattice-asymmetric translation is applied toward AB stacking in the presence of a reflection and time-reversal symmetry, the minimum band gaps occur along $k_\parallel$ and are located exactly at the same energy. This means that the critical field for opening a gap is infinitesimally small. The perturbational results on the size of the band gap are summarized in Table I. As an example, the fourth row in the AA block of Fig. 2 shows a small band gap of ~10 meV (see the inset) for an asymmetric translation of 0.3 Å and an E field of 0.5 eV/Å.

Changes in band structures for around-AA' stacking are well pronounced in the $k_\parallel = 0$ plane (the blue lines in the second and fourth rows of the AA' block in Fig. 2). Of the four bands in that plane, only different Dirac cones can be coupled by a translation. In contrast, under sublattice-symmetric translation, only parallel-band pairs of each Dirac cone are coupled, resulting in a balanced repulsion between them. On the other hand, under sublattice-asymmetric translation, only non-parallel-band pairs of each cone are coupled, which induces an unfavorable crossing. In this slice, the E field only couples parallel-band pairs for sublattice-symmetric translation. Though the crossing point in a Dirac cone does not open, each Dirac cone's crossing band now has a small component of the opposite Dirac cone.

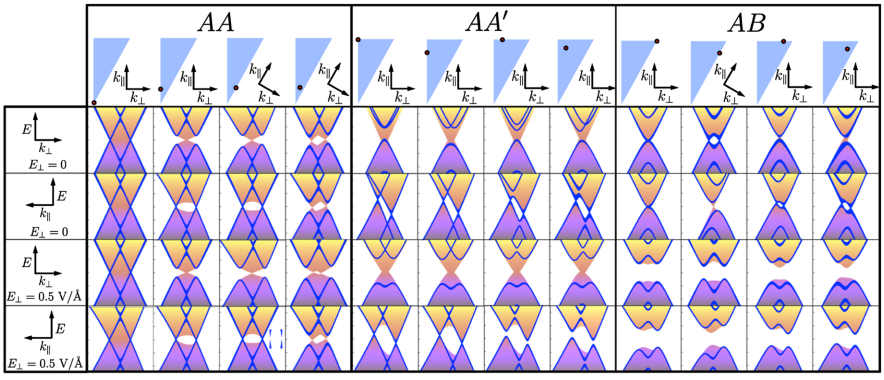

FIG. 2 (color online). Projected band structures around the K point. Each configuration is represented by the translation vector in the irreducible zone of the lattice Wigner-Seitz cell (triangle), where the lower vertex defines the origin. $k_\parallel$ and $k_\perp$ are defined for each configuration. Energy (k space) ranges from −0.5 (−0.2 Å^{-1}) to 0.5 eV (0.2 Å^{-1}) relative to the Fermi level (K). Band structures near the high-symmetry stackings are projected onto the $k_\parallel$-energy and $k_\perp$-energy planes without and with an E field. The inset in the third column of AA stacking highlights a small band gap (≈10 meV).

TABLE I. Analytic expressions of (pseudo)gaps when a small translation x from reference stacking configurations is combined with an interlayer potential difference U, where $\Delta D_{E(k)}$ denotes the energy (crystal momentum) separation of two Dirac points.

Reference	AA	AA'	AB
Translation direction	Toward AB	Toward AB	Any direction
(Pseudo)gap	$\hbar v_F[\Delta D_k(x)/2\Delta D_E(x)]U$	$[\Delta\tilde{\gamma}(x)/\Delta D_E(x)]U$	$(\tilde{\gamma}_{AB}/\sqrt{\tilde{\gamma}_{AB}^2+U^2})U$
	$\hbar v_F = 5.4$ eV Å	$\Delta\tilde{\gamma}(x) \equiv \mathrm{Re}\{\exp[-(2\pi/3)i][(\tilde{\gamma}_{AB}-\tilde{\gamma}_{BA})/2]\}$	$\tilde{\gamma}_{AB} = 0.30$ eV
Parameters	$\Delta D_k(x) = 0.03x$ Å^{-2}	$0.2x < \Delta\tilde{\gamma}(x) < 0.3x$ (eV/Å)	
	$\Delta D_E(x) = 0.68$ eV	$\Delta D_E(x) = 0.22$ eV	
U ($E = 0.5$ V/Å)	0.15 eV	0.52 eV	0.55 eV

Under an E field with sublattice-symmetric stacking, crossing bands still remain crossed, because one crossing band does not have a component parallel to the other crossing band. But if an E field is applied to sublattice-asymmetric stacking, each crossing band now has a small component parallel to the other crossing bands, which opens a small band gap. In spite of Dirac cones opening, the energy level of each Dirac point is different (the fourth row in the AA' block of Fig. 2); thus, a relatively strong E field is required to change this pseudogap into a true gap.

Finally, we move on to the properties of around-AB stacking. As the stacking deviates from exact AB, the doubly degenerate states at the K point immediately split into two crossing points (the second and third columns of the AB block in Fig. 2). From a symmetry viewpoint, the threefold rotational symmetry of monolayer graphene is recovered in AA- and AB-stacked BLG. Combined with translational symmetry, this imposes a threefold symmetry around the K point. Because two separated crossing points are not compatible with the symmetry, wave function symmetries change during the merging of two crossing points [21]. Around AB stacking, an E field opens a band gap. Especially from the eigenvalues of the Hamiltonian, the band gap is $(\tilde{\gamma}_{AB}/\sqrt{\tilde{\gamma}_{AB}^2+U^2})U$, where $\tilde{\gamma}_{AB} = \gamma_{AB} = 0.30$ eV. All the perturbational results for the band gap are summarized in Table I.

Figure 3(a) presents the stacking-dependent band gap under a perpendicular E field of 0.5 V/Å. A sizable band gap opens only around AB stacking, while the rest remains metallic. As the E field goes to zero, the metal-semiconductor phase boundary approaches the line connecting AA and AB stacking, and the entire region becomes metallic. Though no band gap opens by a pure translation, a minute band gap (< 7 meV) was reported [22]

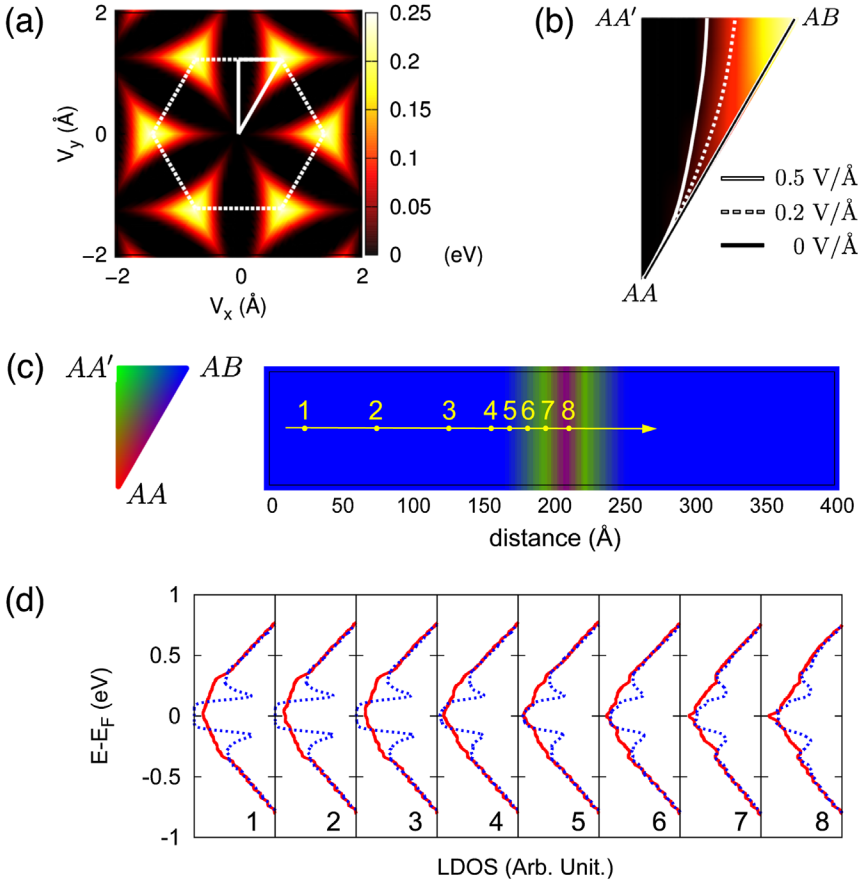

FIG. 3 (color online). (a) A stacking-dependent band gap under a perpendicular E field of 0.5 V/Å. A lattice Wigner-Seitz cell is shown by broken lines and an irreducible zone by solid lines. (b) Metal-semiconductor phase boundaries for different electric field strengths are shown for the irreducible zone. (c) Local stacking configurations of simulated structure are represented by colors in the triangle at the left. (d) Local densities of states of the spotted region in (c) are plotted from the left with (dotted line) and without (solid line) an E field.

for a specific rotation angle without any E field. To investigate the effect of the non-AB-stacking region on the transport property, we constructed an atomic model of a stacking domain boundary with a transition length of 50 Å [Fig. 3(c)]. Tight-binding parameters are assigned to each atom according to its local stacking configuration [23]. When 0.5 eV of on-site energy difference between two layers is applied (0.5 V/Å of E field), a band gap opens at the AB-stacking region, while there remains finite density of states at the non-AB-stacking region [Fig. 3(d)]. This indicates that a high density of midgap states is localized along stacking boundaries even under a strong E field. Because the apparent transport gap is actually estimated from the activation energy of the carrier, a conduction through these midgap states can explain the small transport gap and the low-temperature hopping transport in dual-gated devices.

In summary, we theoretically investigated stacking-dependent gap-opening properties of symmetry-broken bilayer graphene and established a band gap phase diagram.

This research was supported by the Center for Nanophase Materials Sciences, Oak Ridge National Laboratory by the Scientific User Facilities Division, Office of Basic Energy Sciences, U.S. Department of Energy. J. R., S. H., and G. K. were supported by (i) the NanoMaterial Technology Development Program (2012M3A7B4049888) through the NRF, funded by the Ministry of Science, ICT and Future Planning; (ii) the Priority Research Center Program (2010-0020207); and (iii) the Basic Science Research Program (2013R1A2009131) through NRF, funded by the Ministry of Education in Korea.

*Corresponding author.
gunnkim@sejong.ac.kr
†Corresponding author.
myoon@ornl.gov

[1] K. S. Novoselov, D. Jiang, F. Schedin, T. J. Booth, V. V. Khotkevich, S. V. Morozov, and A. K. Geim, Proc. Natl. Acad. Sci. U.S.A. **102**, 10451 (2005).
[2] K. I. Bolotin, K. J. Sikes, Z. Jiang, M. Klima, G. Fudenberg, J. Hone, P. Kim, and H. L. Stormer, Solid State Commun. **146**, 351 (2008).
[3] H. K. Min, B. Sahu, S. K. Banerjee, and A. H. MacDonald, Phys. Rev. B **75**, 155115 (2007); E. McCann, Phys. Rev. B **74**, 161403(R) (2006).
[4] T. Ohta, A. Bostwick, T. Seyller, K. Horn, and E. Rotenberg, Science **313**, 951 (2006); K. F. Mak, C. H. Lui, J. Shan, and T. F. Heinz, Phys. Rev. Lett. **102**, 256405 (2009); Y. B. Zhang, T. T. Tang, C. Girit, Z. Hao, M. C. Martin, A. Zettl, M. F. Crommie, Y. R. Shen, and F. Wang, Nature (London) **459**, 820 (2009).
[5] T. Taychatanapat and P. Jarillo-Herrero, Phys. Rev. Lett. **105**, 166601 (2010).
[6] J. B. Oostinga, H. B. Heersche, X. Liu, A. F. Morpurgo, and L. M. Vandersypen, Nat. Mater. **7**, 151 (2007); T. Taychatanapat and P. Jarillo-Herrero, Phys. Rev. Lett. **105**, 166601 (2010); J. Velasco Jr, Y. Lee, Z. Zhao, L. Jing, P. Kratz, M. Bockrath, and C. N. Lau, Nat. Nanotechnol. **7**, 156 (2012); A. Varlet, M. H. Liu, V. Krueckl, D. Bischoff, P. Simonet, K. Watanabe, T. Taniguchi, K. Richter, K. Ensslin, and T. Ihn, Phys. Rev. Lett. **113**, 116601 (2014).
[7] S. Tanabe, Y. Sekine, H. Kageshima, M. Nagase, and H. Hibino, Jpn. J. Appl. Phys. **50**, 04DN04 (2011).
[8] J. Lin, W. Fang, W. Zhou, A. R. Lupini, J. C. Idrobo, J. Kong, S. J. Pennycook, and S. T. Pantelides, Nano Lett. **13**, 3262 (2013).
[9] J. S. Alden, A. W. Tsen, P. Y. Huang, R. Hovden, L. Brown, J. Park, D. A. Muller, and P. L. McEuen, Proc. Natl. Acad. Sci. U.S.A. **110**, 11256 (2013).
[10] H. Hibino, S. Mizuno, H. Kageshima, M. Nagase, and H. Yamaguchi, Phys. Rev. B **80**, 085406 (2009).
[11] K. S. Kim, A. L. Walter, L. Moreschini, T. Seyller, K. Horn, E. Rotenberg, and A. Bostwick, Nat. Mater. **12**, 887 (2013).
[12] J. P. Perdew, K. Burke, and M. Ernzerhof, Phys. Rev. Lett. **77**, 3865 (1996).
[13] G. Kresse and D. Joubert, Phys. Rev. B **59**, 1758 (1999).
[14] G. Kresse and J. Furthmuller, Phys. Rev. B **54**, 11169 (1996).
[15] A. Tkatchenko and M. Scheffler, Phys. Rev. Lett. **102**, 073005 (2009).
[16] We use extremely dense grid points (0.001 $Å^{-1}$ grid spacing) to ensure an energy resolution up to 5 meV. Maximally localized Wannier functions are constructed from the Bloch functions of uniformly sampled $36 \times 36 \times 1k$ points in the Brillouin zone. In the energy range of ± 2 eV from the Fermi level, first-principles band structures at the sampled k points are exactly reproduced in this interpolation scheme.
[17] N. Marzari and D. Vanderbilt, Phys. Rev. B **56**, 12847 (1997); I. Souza, N. Marzari, and D. Vanderbilt, Phys. Rev. B **65**, 035109 (2001).
[18] See Supplemental Material at http://link.aps.org/supplemental/10.1103/PhysRevLett.115.015502 for the discussion about hopping parameters and the derivation of Table 1, which includes Ref. [19].
[19] N. Marzari, A. A. Mostofi, J. R. Yates, I. Souza, and D. Vanderbilt, Rev. Mod. Phys. **84**, 1419 (2012).
[20] A real space interlayer hopping parameter γ is related to the k space one $\tilde{\gamma}$ by
$$\tilde{\gamma}_{lm} = \sum_{\mathbf{R}_l, \mathbf{R}_m} e^{iK\cdot(\mathbf{R}_m - \mathbf{R}_l)} \gamma_{(l,\mathbf{R}_l)(m,\mathbf{R}_m)},$$
where l and m denote sublattice indices, $\mathbf{R}_{l(m)}$ denotes the position vector of the $l(m)$ sublattice atom, $K = [(2\pi/3a), (2\pi/\sqrt{3}a)]$, and a is the C—C bond length.
[21] Y.-W. Son, S.-M. Choi, Y. P. Hong, S. Woo, and S.-H. Jhi, Phys. Rev. B **84**, 155410 (2011).
[22] S. Shallcross, S. Sharma, and O. A. Pankratov, Phys. Rev. Lett. **101**, 056803 (2008).
[23] Based on the uniformly sampled 487 stacking configurations, we extract the exact hopping parameters and truncated them up to nearest-interlayer pairs. The grid data of hopping parameters are used in the linear interpolative mapping to each atom with the same local stacking configuration. Two hundred k points along the boundary are sampled for the density of states calculations.